Switching of easy-axis to easy-plane anisotropy in cobalt(II) complexes

Yuewei Wu, Jing Xi, Tongtong Xiao, Jesús Ferrando-Soria, Zhongwen Ouyang, Zhenxing Wang, * Shuchang Luo, Xiangyu Liu *
and Emilio Pardo *c

Abstract

Under the guidance of *in situ* microcalorimetry, a tetranuclear cubane-type complex $[Co_4(ntfa)_4(CH_3O)_4(CH_3OH)_4]$ (**1**) with a {Co4O4} core, and a mononuclear complex $[Co(ntfa)_2(CH_3OH)_2]$ (**2**) have been manipulated by adjusting the ratio of the *β*-diketonate and Co(II) ions. Then, the use of three N-donor coligands, 2,2'-bipyridyl (bpy), 6,6'-dimethyl-2,2'-bipyridyl (6,6-$(CH_3)_2$-bpy) and 5,5'-dimethyl-2,2'-bipyridyl (5,5-$(CH_3)_2$-bpy), replaces two coordinated CH_3OH molecules in **2**, leading to three new configurations of **3**-**5**, $[Co(ntfa)_2(bpy)_2]$ (**3**), $[Co(ntfa)_2(6,6\text{-}(CH_3)_2\text{-}bpy)_2]$ (**4**) and $[Co(ntfa)_2(5,5\text{-}(CH_3)_2\text{-}bpy)_2]$ (**5**). Although X-ray crystallography shows that complexes **2**-**5** are mononuclear with distorted octahedral geometries around the Co^{II} ions, the introduction of different capping coligands fine-tunes the structures involving changes in both the distortion degree of the coordination geometry and the intermolecular interactions, which has impact on magnetic properties of these complexes. Magnetic investigations reveal field-induced single-ion magnet behavior in all complexes with distinct energy barriers U_{eff} of 39.06 K (**1**), 36.65 K (**2**), 36.32 K (**3**), 28.26 K (**4**) and 15.85 K (**5**). Remarkably, magnetic experiments, HF-EPR measurements and theoretical calculations demonstrate that **2** features easy-axis magnetic anisotropy (D = -60.48 cm^{-1}), whereas the easy-plane magnetic anisotropies are observed in complexes **3**-**5** with D = +72.85 cm^{-1} for **3**, +35.71 cm^{-1} for **4**, +51.28 cm^{-1} for **5**. To our knowledge, such reversal of anisotropic nature driven by alternative coligands is unprecedented.

Introduction

Single-molecule magnets (SMMs) have been intensively studied for more than two decades due to their significant potential applications in high-density spin-based information storage and spintronics.[1] Historically, SMMs were transition metal containing polynuclear complexes possessing a high spin ground state associated with magnetic anisotropy leading to an energy barrier to the reorientation to their magnetization. More recently, research has been turned to mononuclear SMMs, which are the so-called single-ion magnets (SIMs) of which the magnetic behaviour primarily arises from the inherent magnetic anisotropy of the metal center.[2] Among 3d-SIMs, Co(II)-based complexes are most interesting because of their non-integer spin ground state which declines the probability of quantum tunnelling of magnetization (QTM).[3]

Investigations on existing mononuclear Co(II)-based SIMs verify that the anisotropic nature and magnitude of Co(II) centers is greatly sensitive to tiny modifications of ligand field and coordination geometry as well as coordination environment. Contrary to traditional SMMs whose axial zero-field splitting (ZFS) parameter is certainly negative, the sign and magnitude of magnetic anisotropy in Co-based SIMs depend on more varied and complex parameters.[4] In this context, as Ruiz and Luis et al. showed for a range of mononuclear Co(II) complexes, strong magnetic anisotropies with both a negative ZFS parameter D ($D < 0$) and an easy-plane anisotropy ($D > 0$) can be obtained for mononuclear Co(II) complexes, and thus, field-induced slow magnetic relaxation can be observed regardless of the sign of the D values.[5] Special attention, for example, has been paid to establishing a magneto-structural correlation based on D for mononuclear hexa-coordinated d^7 complexes, especially those Co(II) SIMs with large positive or negative D values.[6] However, even though a remarkable number of Co(II)-based SIMs have been reported so far and great efforts have been made towards finding a solid conceptual explanation for this behavior, the parameters governing magnetic anisotropy are still poorly understood and the daunting task of having precise control

over the magnetic anisotropy remains a difficult challenge.

It is well-established that metal complexes are prepared using complicated multicomponents and heterophase systems in which unobservable physico-chemical processes occur. Selecting suitable ligands is one of the important factors in forming the desirable ligand fields and impacting the magnetic property for resulting complexes. As ideal candidate, *β*-diketonate and its derivatives have been considered to fabricate monometallic complexes and thus trigger the single-ion magnetic anisotropy resulting from their intrinsic characteristics of stable bidentate modes chelating to metal ions and offering proper ligand fields.[7] Meanwhile, the introduction of capping N-donor ligands into the *β*-diketonate-metal systems is beneficial to obtain novel complexes with O_h symmetry and modify their SIM properties.[8] Besides, the structural formation of a compound is often perturbed by the intricate synthetic conditions. A crucial problem is how to predict and manipulate the formation process of targets.

In view of the coordination geometry of hexa-coordinated Co(II) SIMs, we employed a *β*-diketonate, namely, 4,4,4-trifluoro-1-(2-naphthyl)-1,3-butanedione (ntfa), to assemble Co(II) complexes with expectant octahedral geometries. Guided by *in situ* microcalorimetry, two closely related complexes, $[Co_4(ntfa)_4(CH_3O)_4(CH_3OH)_4]$ (**1**) and $[Co(ntfa)_2(CH_3OH)_2]$ (**2**) have been successfully synthesized. Subsequently, **2** could be identified as the precursor contributing to the formation of $[Co(ntfa)_2(bpy)_2]$ (**3**), $[Co(ntfa)_2(6,6\text{-}(CH_3)_2\text{-}bpy)_2]$ (**4**) and $[Co(ntfa)_2(5,5\text{-}(CH_3)_2\text{-}bpy)_2]$ (**5**), while the coordinated CH_3OH solvents are substituted by different capping N-donor coligands. Interestingly, a combination of magnetism, high-frequency electron paramagnetic resonance (HF-EPR) spectroscopy and *ab initio* calculation confirms that complex **2** presents easy-axis magnetic anisotropy, whereas easy-plane magnetic anisotropies are exhibited with other three mononuclear complexes. Moreover, all complexes are indicative of the field-induced slow magnetic relaxation.

Experimental

Materials and methods

Elemental analysis was recorded on a Perkin-Elmer 2400 CHN analyzer. IR spectra were implemented on an EQUINOX55 FT-IR spectrophotometer by using KBr pellets,

in the range 400-4000 cm^{-1}. Powder X-ray diffraction (PXRD) measurements were recorded on a Rigaku RU200 diffractometer at Cu-K_α radiation (λ = 1.5406 Å) with a step size of 0.02° in 2θ and a scan speed of 5° min^{-1}. The calorimetric experiment was performed by using a RD496 type microcalorimeter.[9] Magnetic experiments were performed with a Quantum Design MPMS-XL7 SQUID magnetometer on polycrystalline samples for all complexes (restrained in eicosane to prevent torqueing at high fields). Alternating current (ac) magnetic susceptibility measurements were also carried out with a Quantum Design Physical Property Measurement System (PPMS). Diamagnetic corrections were evaluated from Pascal's Tables. High frequency/field electron paramagnetic resonance (HF-EPR) were measured on a locally developed instruments at the Wuhan National High Magnetic Field Center with pulsed magnetic fields.[10]

Synthesis of [$Co_4(ntfa)_4(CH_3O)_4(CH_3OH)_4$] (**1**). To a solution of ntfa (79.9 mg, 0.3 mmol) in methanol (15 mL) was added Et_3N (0.014 mL, 0.1 mmol). After stirring for 30 min, $CoCl_2 \cdot 6H_2O$ (71.4 mg, 0.3 mmol) were added to the solution, which was stirred for 24 h at room temperature. The filtrate was allowed to stand at room temperature, orange crystals had formed after five days and were collected by filtration. Yield: 81%. Anal. calcd for $C_{40}H_{38}CoF_4N_4O_6$ (M = 805.67). **1**: C 59.63, H 4.75%. Found: C 59.60, H 4.72, N 6.90%. IR data (KBr, cm^{-1}): 3429(w), 3059(w), 2927(w), 1620(m), 1516(m), 1287(m), 1190(m), 1135(s), 1115(s), 801(m), 760(m), 592(w).

Synthesis of [$Co(ntfa)_2(CH_3OH)_2$] (**2**). Complex **2** was prepared by the similar way of **1**, while the ratio of $CoCl_2 \cdot 6H_2O$/ntfa is altered to be 1:2. Yellow crystals of **2** were obtained for 10 days (Yield 63%, based on Co). Anal. calcd for $C_{30}H_{24}CoF_6O_6$ (M = 653.42): C, 55.14; H, 3.70%. Found: 55.08; H, 3.57%. IR (KBr, cm^{-1}): 3060(w), 1614(s), 1596(s), 1535(s), 1300(s), 1254(m), 1200(m), 1139(m), 795(m), 691(m), 584(w), 521(w).

Synthesis of Co(ntfa)$_2$(X) [X = bpy (3), 6,6-$(CH_3)_2$-bpy (4), 5,5-$(CH_3)_2$-bpy (5)]. These complexes were prepared as **2**, but two CH_3OH molecules was replaced by the capping ligand X (X = bpy, 6,6-$(CH_3)_2$-bpy and 5,5-$(CH_3)_2$-bpy). Data for **3**: yield: 75% (based on Co); Anal. calcd for $C_{38}H_{24}CoF_6N_2O_4$ (M = 745.52): 61.22; H, 3.25; N, 8.58%;

Found: C, 61.09; H, 3.12; N, 8.48%; IR (KBr, cm^{-1}): 3432(w), 2925(w), 1605(m), 1298(m), 1128(s), 867(w), 790(w), 689(w), 637(m), 619(s), 471(w). Data for **4**: yield: 67% (based on Co); Anal. calcd for $C_{40}H_{28}CoF_6N_2O_4$ (M = 773.57): C, 62.11; H, 3.65; N, 8.27%; Found: C, 62.03; H, 3.51; N, 8.22%; IR (KBr, cm^{-1}): 3337(w), 1610(s), 1592(s) 1559(s), 1533(m), 1297(s), 1203(s), 1145(s), 1022(m), 855(m), 797(s), 691(m), 582(m). Data for **5**: yield: 65% (based on Co); Anal. calcd for $C_{40}H_{28}CoF_6N_2O_4$ (M = 773.57): C, 62.11; H, 3.65; N, 8.27%, Found: 62.06; H, 3.53; N, 8.20%; IR (KBr, cm^{-1}): 1611(s), 1592(s) 1569(m), 1534(m), 1292(s), 1203(s), 1139(s), 1022(m), 797(s), 591(m).

X-ray crystallography

Suitable crystals of both complexes were selected for X-ray measurements. Crystal structures were collected with a Bruker SMART APEX-CCD-based diffractometer using graphite monochromated Mo-K_α radiation (λ = 0.71073 Å). Data processing and absorption corrections were accomplished using SAINT and SADABS.[11] The structures were solved by direct methods and refined against F^2 by full-matrix least-squares with SHELXTL-2014.[12] All non-hydrogen atoms were refined with anisotropic thermal parameters. All hydrogen atoms were placed in calculated positions and refined isotropically. Crystallographic data for all complexes is provided in Table S1. Selected bond lengths and angles are listed in Tables S2-S6.

Theoretical methods

The theoretical calculations were performed with the ORCA 4.2.1 computational package.[13] Based on X-ray by comparing geometries, B3LYP DFT functional[14] was used for calculations of the magnetic exchange constants J by comparing the energies of high-spin (HS) and broken-symmetry spin (BS) states. The polarized triple-ζ quality basis set def2-TZVP proposed by Ahlrichs and co-workers was used for all atoms.[15] The single-ion zero-field splitting parameters and g-factors were calculated using the state average complete active space self-consistent field (SA-CASSCF)[16] wave functions complemented by the N-electron valence second order perturbation theory (NEVPT2) with CAS(7,5) active spaces. [17] In the state averaged approach all multiplets for the given electron configuration were equally weighted, which means 10 quartet

and 40 singlet states. The ZFS parameters, based on dominant spin-orbit coupling contributions from excited states, were calculated through the quasi-degenerate perturbation theory (QDPT),[18] in which approximations to the Breit-Pauli form of the spin-orbit coupling operator (SOMF approximation)[19] and the effective Hamiltonian theory were utilized.[20] In all calculations, the polarized triple-ζ quality basis set def2-TZVP(-f) proposed by Ahlrichs and co-workers was used for all atoms.[15] The calculations utilized the RI approximation with the decontracted auxiliary def2-TZVP/C Coulomb fitting basis set[21] and the chain-of-spheres (RIJCOSX) approximation to exact exchange.[22] Increased integration grids (Grid6) and tight SCF convergence criteria were used in all calculations.

Results and discussion

Synthesis and thermodynamic behaviors for 1 and 2

In general, the influence of the reaction conditions on the reaction processes is considerable, which may produce the diversity of structures in a specific system. To better govern and cognize the synthetic processes of resulting products, a detailed study on the chemical reaction is of great significance. It is known that *in situ* microcalorimetry is a powerful tool for investigation of thermal events during the reaction processes,[23] which would provide essential thermodynamics support to understand the self-assembly mechanism. Therefore, we online monitored the reaction processes using *in situ* microcalorimetry and quantitatively obtained the apparent energy change for the syntheses.[24] When the molar ratio of metal ions with ntfa is adopted to be 1:1, the reaction system on-time monitored by a microcalorimeter shows that there is one obvious exothermic peak with Q value of 286.6 mJ. By reducing the concentration of cobalt ions to 50%, it is observed that the Q value minishes to 92.9 mJ, less than half of the former. Correspondingly, the response time of the latter process is 95 seconds that is distinctly shorter than that of the former process (175 s). From this point of view, the observation suggests that the reaction system implies two completely different assembly behaviours, portending the formations of two different products, respectively. As described above, the reaction of $CoCl_2 \cdot 6H_2O$ with ntfa in a 1:1 molar

ratio affords single crystals of **1**, whereas complex **2** is prepared in a 1:2 metal to ntfa molar ratio. By means of varying the ratios of cobalt(II) and ntfa, the formation of complexes allowed us to obtain tetranuclear (**1**) and mononuclear (**2**) cobalt(II) species.

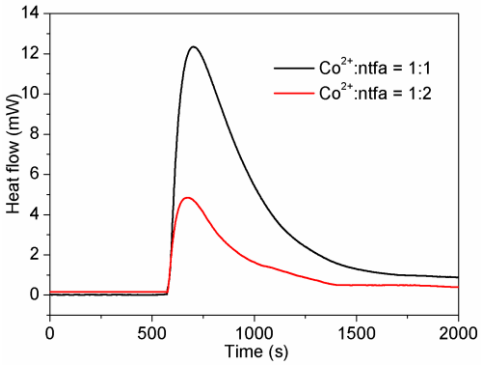

Fig. 1 The black and red lines represent the Heat-flow curve of the mixture of $CoCl_2 \cdot 6H_2O$ and ntfa in 1:1 and 1:2 molar ratio, respectively.

Crystal Structure

X-ray structural analysis reveals that complex **1** is tetranuclear structure that crystallize in the monoclinic space group $P2_1/c$ (Table S1). The molecule has a distorted cubane-type $\{Co_4O_4\}$ core with four six-coordinated Co^{II} atoms occupying four alternating corners of the cube and the other corners are occupied by oxygen atoms of MeOH molecules (Fig. 2a). The overall arrangement has an approximate S_4 symmetry. Similar to the DPM analogue, [25] the cuboidal core is distorted, with all the O-Co-O angles are smaller than 90°, while all Co-O-Co angles are greater than 90° (Fig. 2b). Moreover, the Co···Co distances in cuboidal core ranging from 3.079 to 3.177 Å (Table S2). Among them, each distorted octahedral Co^{II} ion is coordinated to three μ_3-OMe molecules, chelated by a bidentate 4,4,4-trifluoro-1-(2-naphthyl)-1,3-butanedione (ntfa) ligand and one methanol molecule.

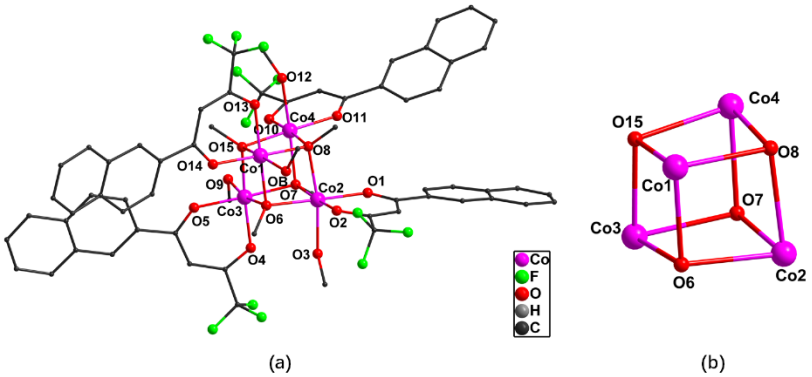

Fig. 2 The asymmetric unit of complex **1** (a) and emphasis of the cubane-like $\{Co_4O_4\}$ fragment of **2**(b). H atoms are omitted for clarity.

X-ray crystallography showed that complexes **2-5** are mononuclear with distorted octahedral geometries around the Co^{II} ions. Complexes **2-4** belong to the triclinic *P*-1 space group, whereas complex **5** crystallize in the monoclinic system with $P2_1/c$ space group (Table S1). The Co^{II} ion in **2** is hexa-coordinated by six O atoms from two ntfa ligands and two methanol molecules (Fig. 3a). The axial Co-O bond distances (2.130 Å) are longer than the equatorial Co-O bond distances (2.035 Å and 2.048 Å), leading to stretched octahedral geometries (Table S3). Evidently, two coordinated CH_3OH molecules in **2** are replaced by 2,2'-bipyridyl (bpy), 6,6'-dimethyl-2,2'-bipyridyl (6,6-$(CH_3)_2$-bpy) and 5,5'-dimethyl-2,2'-bipyridyl (5,5-$(CH_3)_2$-bpy) ligands, forming the configurations of **3-5**. Consequently, the Co^{II} centers in **3-5** link with six donor atoms consisting of four O atoms from two ntfa ligands and two N atoms from neutral coligands (Fig. 3b-3d). For **3-5**, the average Co-O bond lengths are 2.06, 2.07 and 2.06 Å, and the average Co-N bond lengths are 2.12, 2.15 and 2.10 Å, respectively (Tables S4-S6). Thus, almost identical Co-O bond lengths are observed for **3-5**. In turn, the Co-N distance for **4** is appreciably greater than that in other two complexes. It is worth noting that the smallest intermetallic distance in complex **2** is 5.238 Å, which illustrates non-negligible intermetallic interaction. In contrast, the metal centers are well-separated with the shortest Co···Co distance of 7.504, 7.189 and 7.531 Å for **3-5**, respectively, thus excluding potential intermolecular dipole-dipole interactions.

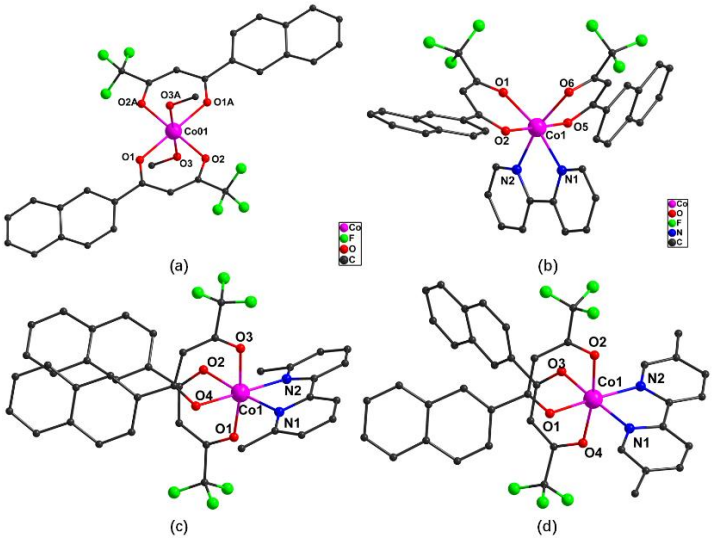

Fig. 3 Crystal structures of **2**(a), **3**(b), **4**(c) and **5**(d) of the Co(II) ions. Hydrogen atoms are omitted for clarity.

The geometric configurations of the Co^{II} cations in **1**-**5** were calculated by using the SHAPE 2.1 program (Tables S7 and S8).[26] The calculated parameter from the software is zero for the ideal structure, and larger values indicate greater deviation from the ideal polyhedron. The investigation of the precise configurations demonstrated that Co^{II} cations in **1**-**5** fit well with the hexa-coordinate octahedral polyhedron with continuous shape measures (CShMs) of 0.445 (Co1), 0.448 (Co2), 0.533 (Co3) and 0.417 (Co4) (**1**), 0.057 (**2**), 1.030 (**3**), 0.857 (**4**) and 0.698 (**5**).

Static (dc) magnetic properties and HF-EPR measurements

Magnetic studies were performed on polycrystalline samples of complexes **1**-**5**, and the phase purity of the bulk materials was confirmed by powder XRD (Fig. S1). Variable-temperature dc magnetic susceptibility data of these complexes were measured in the 2-300 K temperature range with an applied field of 1000 Oe. For complex **1**, as shown in Fig. 4a, $\chi_M T$ rises slowly from 13.98 cm^3 K mol^{-1} with decreasing temperature, then increases sharply to a maximum of 17.14 cm^3 K mol^{-1} at 10 K, finally rapidly drops to 15.04 cm^3 K mol^{-1} at 2 K. From the value of the peak at 10 K, it appears that all four Co^{2+} ions are ferromagnetically coupled to give an $S = 6$ ground state. The decrease in $\chi_M T$ below 10 K is probably due to zero-field splitting,[27] and also due to the more common complications arising from spin-orbital interaction,[28] which is a frequent source of difficulty in the interpretation of magnetic data for Co^{2+}

complexes.

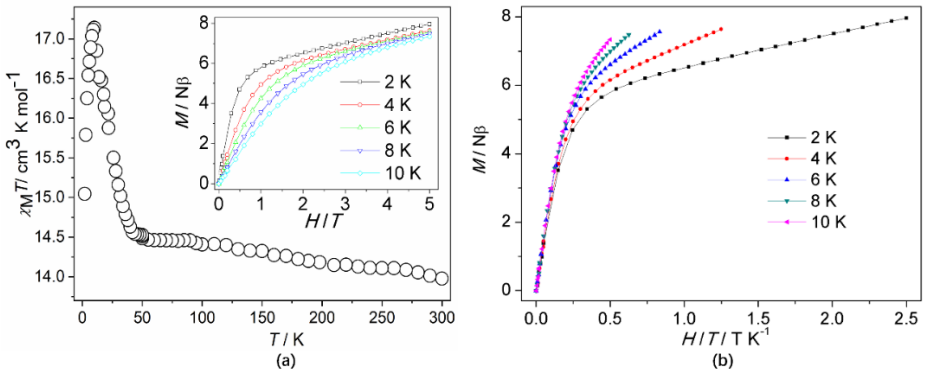

Fig. 4 Plots of $\chi_M T$ versus T for complex **1**(a). Inset: The experimental plots of M versus H at different temperatures. Plots of M vs H/T for **1**(b) at different temperatures.

At room-temperature, the $\chi_M T$ values of **2-5** are 3.52 cm^3 K mol^{-1}, 2.53 cm^3 K mol^{-1}, 3.11 cm^3 K mol^{-1} and 2.89 cm^3 K mol^{-1}, respectively. These values are clearly larger than the spin-only value (1.875 cm^3 K mol^{-1}) for a magnetically isolated Co(II) cation (S = 3/2 and g = 2.0), indicating a significant orbital contribution to the magnetic moment. Upon cooling, the $\chi_M T$ values decreases monotonously to 2 K, reaching 2.37, 1.45, 1.88 and 1.66 cm^3 K mol^{-1} for **2-5**, respectively. The field-dependent magnetizations in the form of the M vs. H plots for **2-5** are represented in the inset of Fig. 5. For these complexes, the M vs. H/T plots at different temperatures are not superimposable (Fig. S2), clearly confirming the presence of a significant magnetic anisotropy, which is derived from the well-known strong spin-orbital coupling (SOC) of the Co(II) ion.[29] To gain insight into the magnetic anisotropy of complexes **2-5**, the reliable ZFS parameters were obtained by simultaneously fitting the experimental M *vs.* H curves using the *PHI* program[30] based on the following spin Hamiltonian of eq (1):

$$\hat{H} = g\mu_B \hat{S} \cdot B + D(\hat{S}_z{}^2 - \hat{S}^2/3) + E(\hat{S}_x{}^2 - \hat{S}_y{}^2) \qquad (1)$$

where μ_B is the Bohr magneton, D is the axial ZFS parameter, E is the rhombic or transverse ZFS parameter, S is the spin operator, and B is the magnetic field vector, respectively. The parameters D, E, and g were selected to correlate the data. The best fit values are summarized with parameters: D = -60.48 cm^{-1}, $|E|$ = 15.27 cm^{-1}, $g_{x,y}$ = 3.56, g_z = 2.20 for **2**, D = +72.85 cm^{-1}, $|E|$ = 11.57 cm^{-1}, g_x = 2.34, g_y = 2.28, g_z = 2.12, for **3**, D = +35.71 cm^{-1}, $|E|$ = 4.81 cm^{-1}, $g_{x,y}$ = 2.14, g_z = 2.12 for **4** and D = +51.28 cm^{-}

[1], $|E|$ = 13.41 cm^{-1}, $g_{x,y}$ = 2.57, g_z = 2.56 for **5**, respectively. Note that the negative sign of the D values for complex **2** illustrates easy axial magnetic anisotropy, whereas the strong easy-plane magnetic anisotropy observed in complexes **3**-**5**.

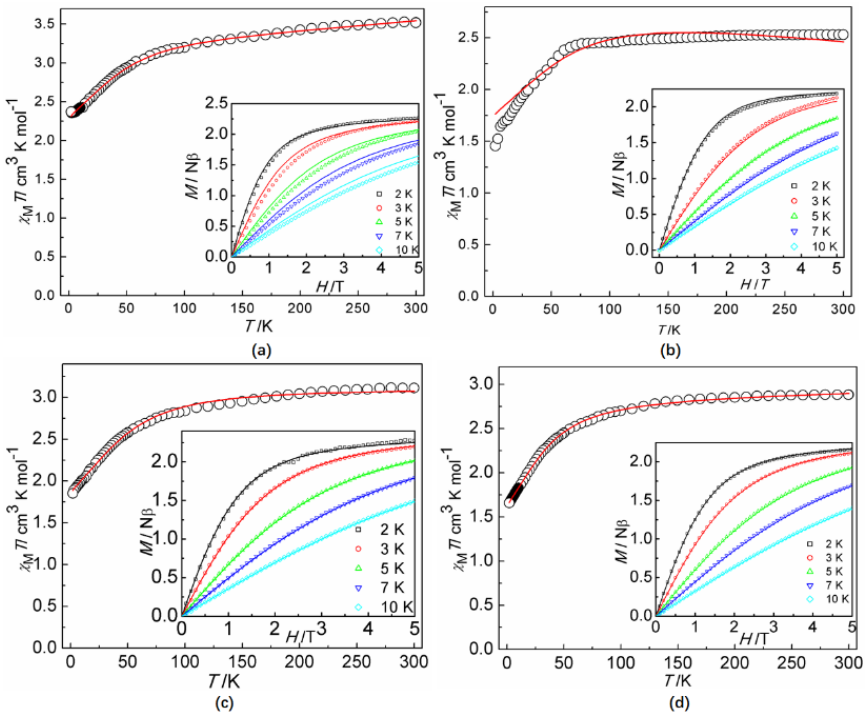

Fig. 5 Plots of $\chi_M T$ versus T for complexes **2**-**5**. Inset: The experimental plots of M versus H at different temperatures. The solid lines show the best-fitting curves to the experimental data.

HF-EPR measurements were recorded on polycrystalline samples of **2**-**5** at frequencies of up to 170 GHz in order to further confirm the ZFS parameters. As shown in Fig 6, we can easily get the EPR spectra containing three main modes, which is the typical feature of a high spin cobalt(II) ion compound with S = 3/2. As expected, like the magnitudes of the D values are out of the frequency range in our measurements, no transitions between Kramers doublets $M_S = \pm 1/2$ and $M_S = \pm 3/2$ were observed (Fig. 6). All the EPR signals can be interpreted as from the intra-Kramers transitions within the lowest doublet $M_S = \pm 1/2$ multiplet with $\Delta M_S = \pm 1$. The relationship of the resonance fields and its corresponding various microwave frequencies curve were shown in Fig. 7. The resonance fields were simulated using the $|D|$ value of 60.48 cm^{-1}, 72.85 cm^{-1}, 51.28 cm^{-1} and 35.71 cm^{-1} from SQUID measurements while adjusting E (transverse zero-field splitting parameter) and g values to get the well-estimated data.

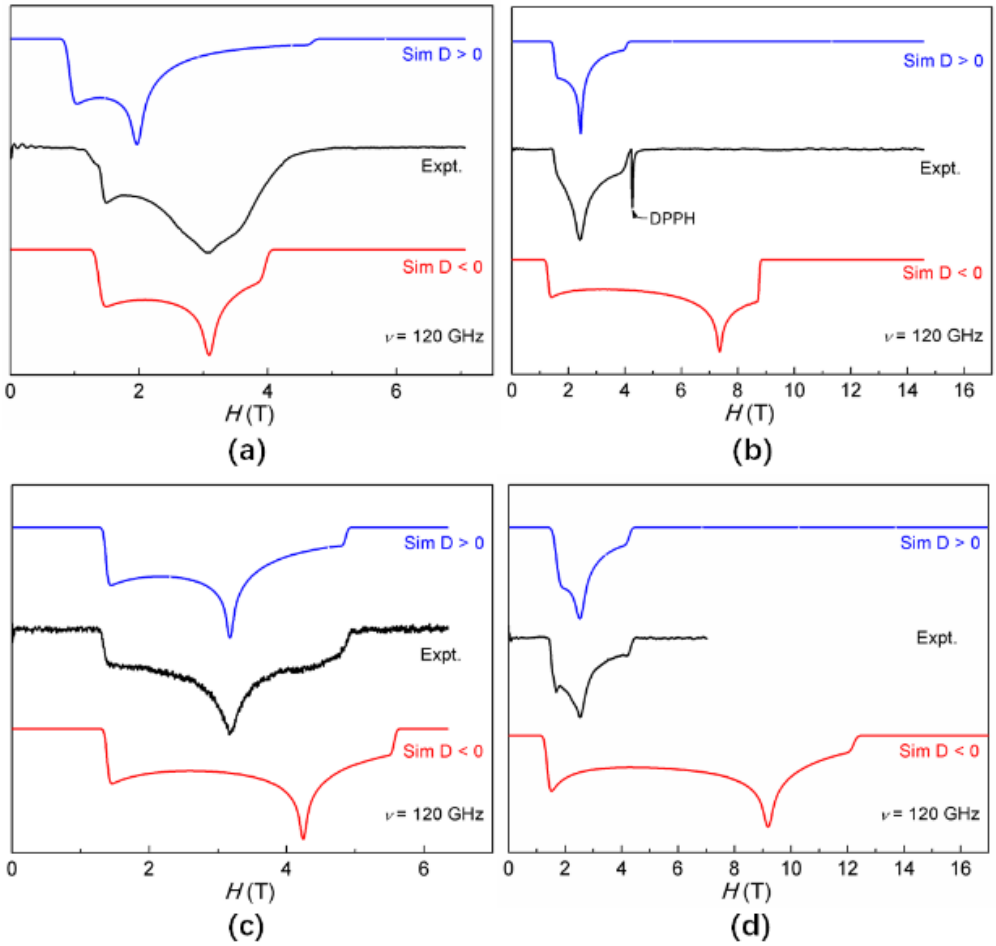

Fig. 6 HF-EPR spectrum of **2**(a), **3**(b), **4**(c) and **5**(d) at 4.2 K and its simulations (blue trace: positive *D*; red trace: negative *D*) at 120 GHz.

For complex **2**, two simulations were done with different signs of *D*, showing that the negative *D* value are well in accord to the experimental data. But beyond that, there are only two peaks in the spectra, which is typical for high-spin 3/2 Co(II) systems with large negative *D* values due to the limit of magnetic field, indicating the easy-axis magnetic anisotropy in **2**.[31] The situation above were confirmed by $[Co(hfac)_2(H_2O)_2]$[32] and $[Co(acac)_2(H_2O)_2]$.[33] In contrast, the simulation with $D > 0$ fit better to the experiment data than did those with $D < 0$ for **3**-**5**, determining that the *D* values are positive. The positive *D* values of **3**-**5** might derive from the spin-orbital coupling of the ground state and excited state electrons, which further demonstrates the easy-plane magnetic anisotropies.

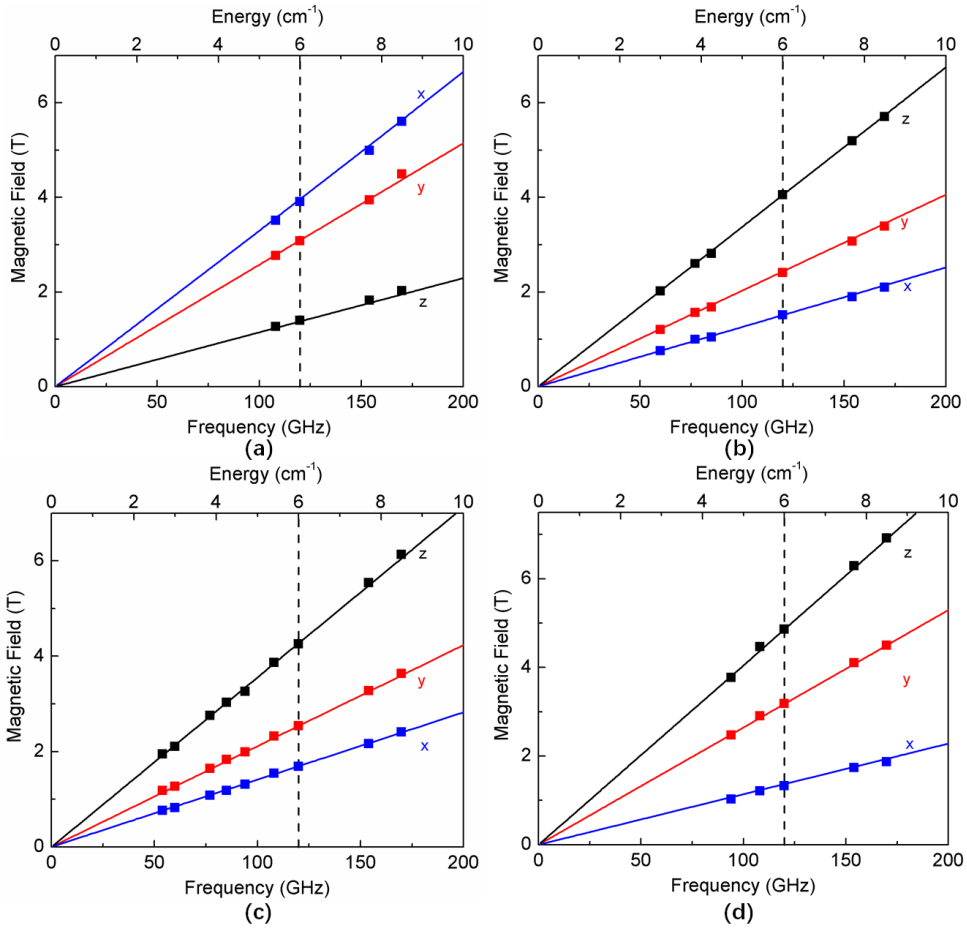

Fig. 7 Resonance field vs. microwave frequency (quantum energy) for EPR transitions for **2**(a), **3**(b), **4**(c) and **5**(d). Simulations were done using the Hamiltonian parameters taken from Fig. 6 The solid lines show the (x, y, z) transitions as labeled. The vertical dashed lines represent the frequency (120 GHz) used in Fig. 6 at which the spectra were recorded or simulated.

Dynamic (ac) magnetic properties

For the purpose of probing the spin dynamics, alternating current (ac) magnetic susceptibility measurements were conducted at zero dc field at a frequency of 1000 Hz. No out-of-phase (χ''_M) signals were observed for all complexes until the temperature dropped to 2 K (Fig. S3), signifying a fast quantum tunneling of the magnetization (QTM) at low temperature. In order to find a suitable applied magnetic field to suppress the QTM, the χ''_M susceptibilities for all complexes at 2.0 K and 1000 Hz were recorded under different magnetic fields. The χ''_M signals with significant peak values at around 2000 Oe dc field suggest that field-induced slow magnetic relaxation and slow

relaxation operate in five complexes. Thus, 2000 Oe was used as a suitable applied field for **1**-**5**, and in-phase and out-of-phase ac susceptibilities were clearly observed. The temperature dependence of in-phase (χ') and out-of-phase (χ'') products were measured in the temperature ranges 2-6 K for complex **1** and 2-10 K for **2**-**5**, respectively (Fig. S4 and S5). The downturn in both the χ' and χ'' susceptibilities in the low temperature range and the appearance of obvious peaks for all complexes indicate that the relaxation probability via the quantum pathway has been obviously weakened or suppressed. At the selected frequency, all complexes go through a maximum and maxima shift to high temperature with increasing frequency, which is characteristic of a superparamagnet.

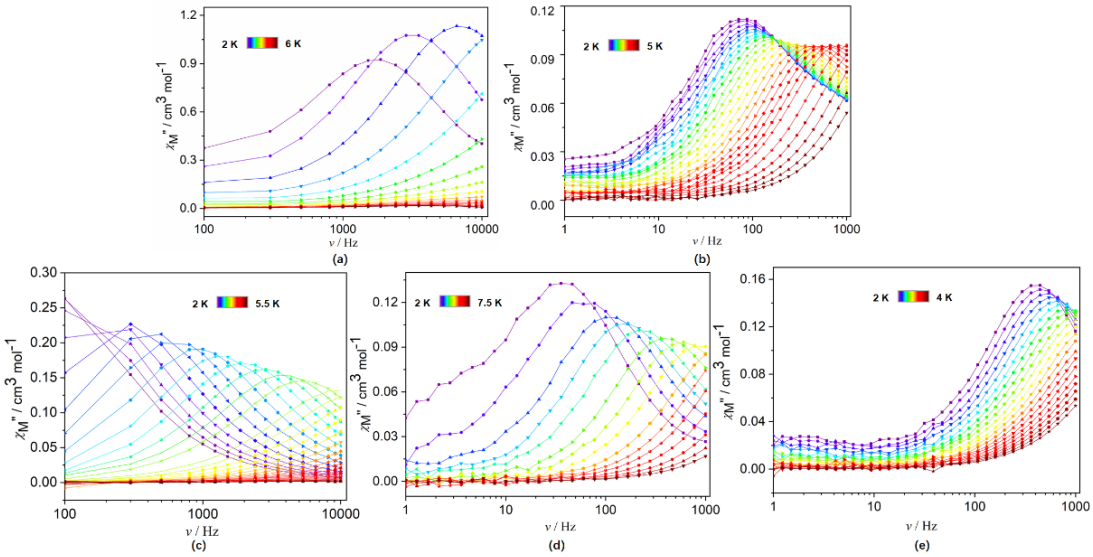

Fig. 8 Frequency dependence of the out-of-phase ac susceptibility signals for complexes **1**-**5** under a 2000 Oe dc field.

In addition, the frequency dependencies of the ac susceptibility were measured under an applied dc field of 2000 Oe (Fig. 8 and S6). Both the χ' and χ'' signals of **1**-**5** appear to be frequency dependent. As the temperature increases, the peaks of χ'' in **1**-**5** gradually shift from low frequency to high frequency. Fitting the high-temperature data using the Arrhenius law $\tau = \tau_0 \exp(U_{eff}/k_B T)$ affords the effective spin-reversal energy barrier (U_{eff}) and pre-exponential factor τ_0 (Fig. 9): **1**, U_{eff} = 30.28 K, $\tau_0 = 5.4 \times 10^{-9}$ s; **2**, U_{eff} = 29.29 K, $\tau_0 = 1.21 \times 10^{-7}$ s; **3**, U_{eff} = 29.74 K, $\tau_0 = 8.1 \times 10^{-8}$ s; **4**, U_{eff} = 25.81 K, $\tau_0 = 7.52 \times 10^{-7}$ s; **5**, U_{eff} = 13.03 K, $\tau_0 = 1.64 \times 10^{-6}$ s. Furthermore, the curvature

that emerged in the Arrhenius plots of five complexes also implies non-negligible direct and/or Raman processes in determining the relaxation rate. Thereby, a model including three possible relaxation processes, i.e. direct, Raman and Orbach mechanisms,[34] was employed to analyze the contribution to the relaxation in **1**-**5** using eqn (1):

$$\tau^{-1} = AT + CT^{n} + \tau_0{}^{-1} exp(-U_{\text{eff}}/kT) \quad (1)$$

where the terms in eqn (1) represent the contributions of multiple mechanisms. For the second term, n = 7 is expected for the Raman process in non-Kramers ions and n = 9 for Kramers ions, while n = 1-6 can occur for the optical acoustic Raman-like process. As depicted in Fig. 9, the fitting reproduces the experimental data very well, resulting in the parameters **1**, A = 611 K^{-1} s^{-1}, C = 83.25 K^{-n} s^{-1}, n = 4.88, τ_0 =1.95 × 10^{-9} s, $\Delta E/k_B$ = 39.06 K; **2**, A = 275 K^{-1} s^{-1}, C = 1.65 K^{-n} s^{-1}, n = 4.92, τ_0 = 3.61 × 10^{-8} s, $\Delta E/k_B$ = 36.65 K; **3**, A = 186 K^{-1} s^{-1}, C = 2.48 K^{-n} s^{-1}, n = 5.56, τ_0 = 5.85 × 10^{-8} s, $\Delta E/k_B$ = 36.32 K; **4**, A = 55.49 K^{-1} s^{-1}, C = 3.42 K^{-n} s^{-1}, n = 4.41, τ_0 = 9.77 × 10^{-7} s, $\Delta E/k_B$ = 28.26 K; **5**, A = 832 K^{-1} s^{-1}, C = 43.18 K^{-n} s^{-1}, n = 3.87, τ_0 = 1.73 × 10^{-6} s, $\Delta E/k_B$ = 15.85 K. For **1**-**3** and **5**, the low temperature region is probably dominated by a direct process, whereas the relaxation process at high temperature can be mainly attributed to an optical acoustic Raman-like mechanism. In the case of **4**, it was observed that the contributions of the Orbach and direct processes are small compared with the optical acoustic Raman process.

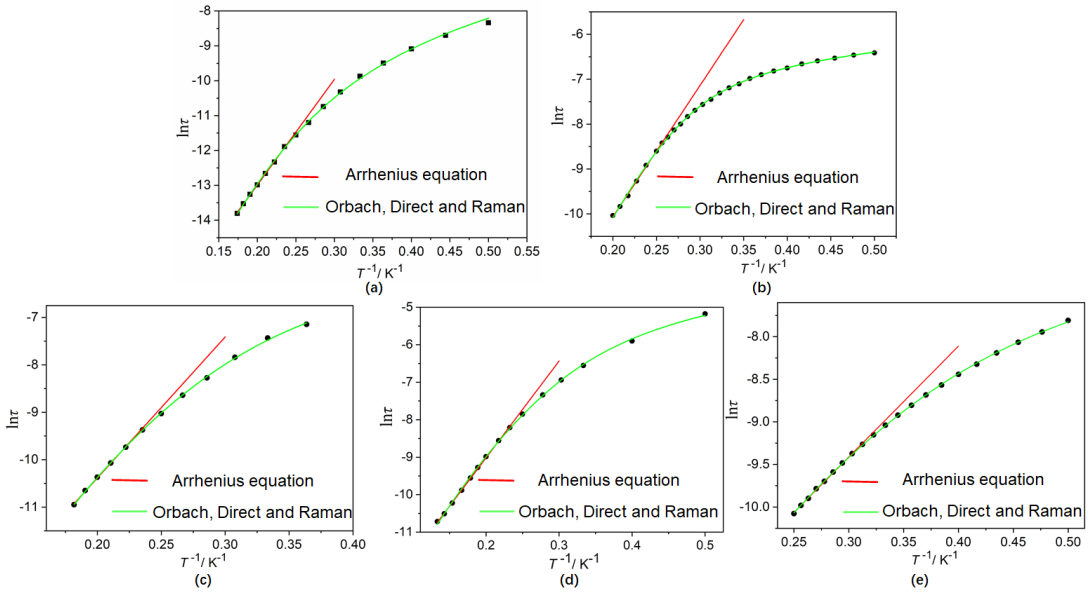

Fig. 9 Magnetization relaxation time, lnτ vs. T^{-1} plot under a 2000 Oe dc field for **1**-**5**. The red and

green lines represent the Arrhenius fit and multiple relaxation processes, respectively.

Cole-Cole diagrams for **1-5** were also obtained (Fig. 10). As shown, individual semicircular shapes can be evidently noticed in the motifs, which could be well-fitted using the generalized Debye model.[35] As listed in Tables S9-S13, the α parameters are 0.10-0.18 for **1**, 0.006-0.014 for **3** and 0.016-0.12 for **4**, suggesting narrow distributions of the relaxation processes. In contrast, the α values are 0.012-0.34 for **2** and 0.013-0.26 **5**, demonstrating a wide distribution of relaxation times.

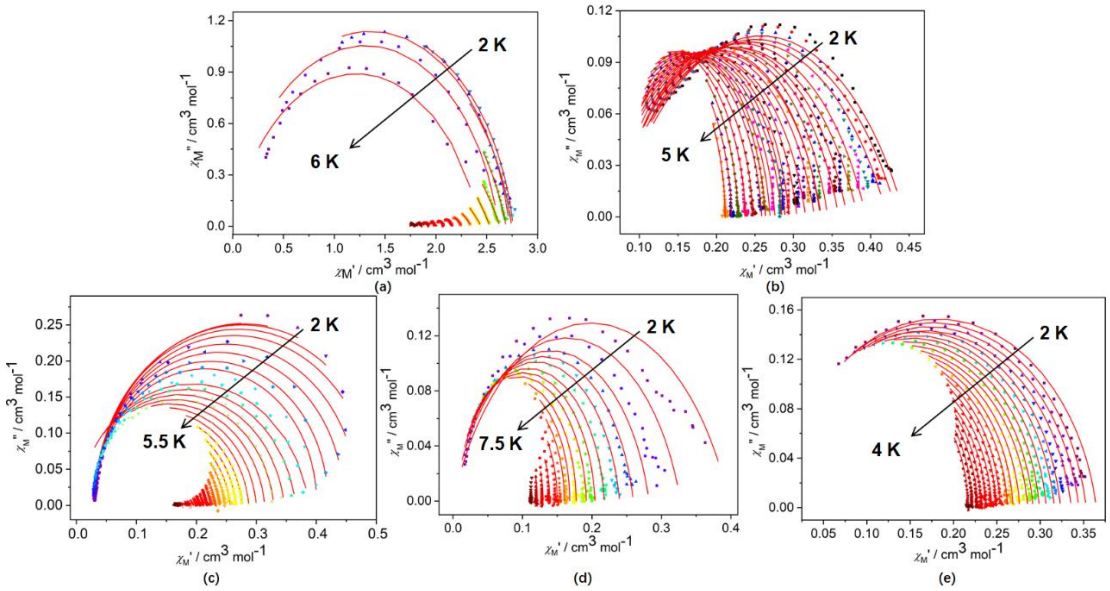

Fig. 10 Cole-Cole plots under 2000 Oe for **1-5**. The solid lines show the best fitting according to the generalized Debye model.

Theoretical calculations

Before the analysis of the experimental magnetic data of five complexes, the predictive role of *ab initio* calculations in magnetochemistry was utilized with the aim of estimating the principal parameters describing the exchange coupling and the zero-field splitting in these molecular systems.[36] Therefore, Density Functional Theory (DFT) was applied to calculate the parameters of the isotropic exchange J between the paramagnetic ions, and the multireference method based on Complete Active Space Self Consistent Field (CASSCF) was utilized to derive information about the single-ion zero-field splitting tensor parameters D and E. Having such information at our disposal,

the trustworthy spin Hamiltonians can be postulated and the calculated parameters can be used as a starting point for fitting of the experimental magnetic data. All theoretical calculations were performed with a freely available computational package ORCA.[13a] All the calculations were done for molecular geometries extracted from X-ray data and also for molecular geometries optimized with the BP86 functional (see the Experimental section for more details).

We carried out DFT calculations on structures **1** to help rationalise the experimental information on molecular magnetism. Since the DFT deals with single Slater determinants to describe open-shell electronic configurations instead of spin-adapted states, we applied the broken-symmetry approach to compute the energies of the open-shell configurations, namely those with $M_S \leq S_{HS}$. By inspection of the structural parameters, we considered a two-*J* model based on the presence of four shorter (J_1) and two longer (J_2) Co···Co distances to determine the sign and magnitude of the magnetic interactions between the local spin moments of Co(II) ions. As deduced from the $\chi_M T$ values at high *T* shown in Fig. 5, the Co(II) ions in **1** are characterised by the local spins of 3/2. Thus, to extract the J_1 and J_2 parameters we computed the three situations depicted in Fig. 11: the high-spin (|ααααα>, $S_{HS} = 6$), the intermediate-spin (|βααα>, $S_{BS1} = 3$) and the low-spin (|βααβ>, $S_{BS2} = 0$) configurations, where each arrow represents spin 3/2 for Co(II). (Fig. 11 and Table S14)[37] The magnetic coupling constant between magnetic centers was modeled using the Heisenberg approach:

$$\hat{H} = -J_1(S_2S_3 + S_3S_4 + S_1S_4 + S_1S_2) - J_2(S_1S_3 + S_2S_4)$$

where each arrow represents spin 3/2 for Co. From this model, the energy spectrum is:

$$E_{HS} = -9J_1 - \frac{9}{2}J_2 \qquad E_{BS1} = 0 \qquad E_{BS2} = 9J_1 - \frac{9}{2}J_2$$

$$\Delta_1^a = E_{BS1} - E_{HS} = 9J_1 + \frac{9}{2}J_2 \qquad \Delta_2^a = E_{BS2} - E_{HS} = 18J_1$$

The calculation details are listed in Table S14 and the spin densities of the HS spin states are shown in Fig. S7 for **1**. The partial spin delocalization from the metal atoms to the respective donor atoms is clearly visible. Next, the *J*-parameters calculated according to eqn (2) adopted the values $J_1 = 5.663$ cm^{-1} and $J_2 = 10.121$ cm^{-1}. Evidently, there are dominant antiferromagnetic interactions in **1**, but there is no simple correlation

of the calculated *J*-parameters with either the Co-O-Co angle or the Co···Co distance.

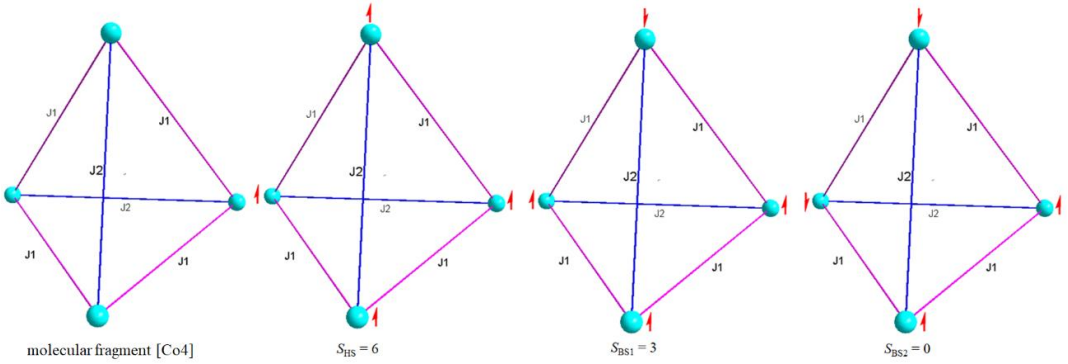

Fig. 11 Three possible orientations of local spin moments (arrows: spin 3/2 for Co) and total (*S*, sum of arrows) spin quantum numbers for the cubane-type Co4 complex. The coupling constants J_1 and J_2 represent the strength of the interactions between the Co ions bridged by μ_3-O ligands. {d_{23}=3.0791, d_{34}=3.0797, d_{12}=3.0899, d_{14}=3.0812(J_1); d_{13}=3.1563, d_{24}=3.1774(J_2)}

Furthermore, in order to better understand the impact of the auxiliary ligands on the electronic structure of the six-coordinate complexes under study, especially on their magnetic anisotropy, post-Hartree-Fock CASSCF calculations were performed. The approach done with ORCA resulted in large *D*-values (-29.30 cm^{-1}, 59.18 cm^{-1}, 51.82 cm^{-1} and 45.73 cm^{-1} for **2**-**5**, respectively) (Table 1). Although the calculated values show a certain deviation from the fitting values, the sign of the *D* constant matches well with the experimental values, which definitely confirms the easy-axis magnetic anisotropy of the complex **2** and easy-plane magnetic anisotropy of **3**-**5**. It is difficult to estimate the accuracy of the theoretical calculations, but the work is only qualitative. This may result from the fact that the real complexes are not made up of scattered entities as they have been modelled, but are very complicated across the whole structures. The calculated effective g_z tensors are 2.365 ($g_{x,y}$ = 2.034, 2.268), 2.669 ($g_{x,y}$ = 2.054, 2.426), 2.666 ($g_{x,y}$ = 2.044, 2.392) and 2.539 ($g_{x,y}$ = 2.071, 2.428) for complexes **2**-**5**, respectively. The energy levels and the contributions of the excited spin states to the *D*-tensors are listed in Tables S15-S22. The results manifest that the first two excited quartets have a significant contribution to the *D* parameters for all complexes.

Table 1 ORCA/CASSCF+NEVPT2 computed *D*, *E*, and g value for complex **2-5**

Complex	*D* (cm^{-1}) (experiment)	*D* (cm^{-1}) (calculation)	*E* (cm^{-1})	g_{iso}	g_x	g_y	g_z
2	-60.48	-29.304	-9.559	2.222	2.034	2.268	2.365
3	72.85	59.179	9.898	2.383	2.054	2.426	2.669
4	35.71	51.822	13.470	2.367	2.044	2.392	2.666
5	51.28	45.731	6.386	2.346	2.071	2.428	2.539

Magneto-structural correlations

To understand the origin of the magnetization dynamics, it is necessary to provide a structural comparison of the coordination spheres for the four mononuclear complexes. Structurally, complex **2** exhibits a CoO_6 chromophore with slightly distortion (CShMs = 0.057) from the ideal octahedron, whereas the Co(II) ions in **3-5** present CoN_2O_4 chromophore with obvious distortion (CShMs = 1.030, 0.857 and 0.658 for **3-5**, respectively) from the corresponding ideal geometry. Consequently, the energy barrier for **2** is larger than that in other three complexes. For **3-5**, the discrepancies of magnetic anisotropy and energy barrier dominantly depends on the different terminal substituents of capping N-donor ligands. Among them, 2,2'-bipyridyl coligand in complex **3** is conducive to promoting the single-ion anisotropy and thus the slow relaxation of the magnetization, achieving enhanced energy barrier, suggesting that the electron-donating $-CH_3$ groups in **4** and **5** produce negative effects on the dynamic magnetic properties. Complexes **4** and **5** containing two isomeric capping N-donor coligands where two $-CH_3$ groups are located on the different positions display distinctly different energy barriers, confirming the significance of the substituent effect on the single-ion behaviour. To further acquire the deep understanding for the variously anisotropic nature of complexes **2-5**, the charge distributions of Co(II) ions and coordination atoms are considered concurrently (Table S23). Evidently, the charge distributions derived from the changes of substituents lead to different bond lengths, which further has a significant effect to alter the distortion degree from the ideal octahedral geometry of the complexes. As a result, the reversals of the anisotropic sign have been observed.

Conclusion

In summary, we report here two completely different Co(II)-containing complexes, $[Co_4(ntfa)_4(CH_3O)_4(CH_3OH)_4]$ (**1**) and $[Co(ntfa)_2(CH_3OH)_2]$ (**2**), that are successfully guided via *in situ* microcalorimetry. Three new mononuclear complexes, $[Co(ntfa)_2(bpy)_2]$ (**3**), $[Co(ntfa)_2(6,6\text{-}(CH_3)_2\text{-}bpy)_2]$ (**4**) and $[Co(ntfa)_2(5,5\text{-}(CH_3)_2\text{-}bpy)_2]$ (**5**), are evolved from **2** through combining the corresponding capping N-donor coligands. Co(II) ions in all cases are encompassed by the octahedral coordination geometries with variously architectural distortions. The coligand effect on the magnetic dynamics and magnetic anisotropy of the octahedral Co(II) centers is systematically investigated. All complexes are characteristic of field-induced slow magnetic relaxation, with energy barriers U_{eff} of 39.06 K (**1**), 36.65 K (**2**), 36.32 K (**3**), 28.26 K (**4**) and 15.85 K (**5**). Excitedly, it is first noted that the coligand-induced structural perturbation reverses the sign of the single-ion anisotropy from easy-axis type for **2** to easy-plane type for **3**-**5**. The outcomes illustrated in this work would offer new possibility for the accurate assessment of controllable preparation by *in situ* microcalorimetry, and provide solid evidence of the effects of coligand variations on magnetic anisotropy and magnetization dynamics in Co(II)-based SIMs, the ultimate goal of which is to advance the deliberate tailoring of SIMs. Further studies following this guideline are actually ongoing.

Acknowledgements

We gratefully acknowledge the financial support from the National Natural Science Foundation of China (21863009, U20A2073), the Natural Science Foundation of Ningxia Province (2020AAC02005), the Discipline Project of Ningxia (NXYLXK2017A04), and the Guizhou Education Department Youth Science and Technology Talents Growth Project (No. KY [2020]158). Thanks are also extended to the 2019 Post-doctoral Junior Leader-Retaining Fellowship, la Caixa Foundation (ID100010434 and fellowship code LCF/BQ/PR19/11700011), the "Generalitat Valenciana" (SEJI/2020/034) and the "Ramón y Cajal" program (J. F.-S.). E. P. acknowledges the financial support from the European Research Council under the

European Union's Horizon 2020 research and innovation programme/ ERC Grant Agreement No. 814804, MOF-reactors.

Notes and references

1. (a) E. Moreno-Pineda, C. Godfrin, F. Balestro, W. Wernsdorfer and M. Ruben, *Chem. Soc. Rev.*, 2018, **47**, 501-513; (b) M. Shiddiq, D. Komijani, Y. Duan, A. Gaita-Ariño, E. Coronado and S. Hill, *Nature*, 2016, **531**, 348-351; (c) J. Ferrando-Soria, J. Vallejo, M. Castellano, J. Martínez-Lillo, E. Pardo, J. Cano, I. Castro, F. Lloret, R. Ruiz-García and M. Julve, *Coord. Chem. Rev.* 2017, **339**, 17–103.
2. (a) X.-Y. Liu, L. Sun, H.-L. Zhou, P.-P. Cen, X.-Y. Jin, G. Xie, S.-P. Chen and Q.-L. Hu, *Inorg. Chem.*, 2015, **54**, 8884-8886; (b) X.-Y. Liu, X.-F. Ma, W.-Z. Yuan, P.-P. Cen, Y.-Q. Zhang, J. FerrandoSoria, S.-P. Chen and E. Pardo, *Inorg. Chem.*, 2018, **57**, 14843-14851.
3. (**a**) J. M. Zadrozny, D. J. Xiao, M. Atanasov, G. J. Long, F. Grandjean, F. Neese and J. R. Long, *Nat. Chem.*, 2013, **5**, 577-581; **(**b**)** Y.-W. Wu, D.-N. Tian, J. Ferrando-Soria, J. Cano, L. Yin, Z.-W. Ouyang, Z.-X. Wang, S.-C. Luo, X.-Y. Liu and E. Pardo, *Inorg. Chem. Front.*, 2019, 6, 848-856; (c) J. M. Zadrozny, M. Atanasov, A. M. Bryan, C.-Y. Lin, B. D. Rekken, P. P. Power, F. Neese and J. R. Long, *Chem. Sci.*, 2013, **4**, 125-138.
4. S. Vaidya, S. Tewary, S. K. Singh, S. K. Langley, K. S. Murray, Y. Lan, W. Wernsdorfer, G. Rajaraman and M. Shanmugam, *Inorg. Chem.*, 2016, **55**, 9564-9578.
5. S. Gomez-Coca, A. Urtizberea, E. Cremades, P. J. Alonso, A. Camon, E. Ruiz and F. Luis, *Nat. Commun.*, 2014, **5**, 4300-4307.
6. Z.-W. Chen, L. Yin, X.-N. Mi, S.-N. Wang, F. Cao, Z.-X. Wang, Y.-W. Li, J. Lu and J.-M. Dou, *Inorg. Chem. Front.*, 2018, **5**, 2314-2320.
7. (a) K. Bernot, J. Luzon, L. Bogani, M. Etienne, E. C. Sangregorio, M. Shanmugam, A. Caneschi, R. Sessoli and D. Gatteschi, *J. Am. Chem. Soc.*, 2009, **131**, 5573-5579; (b) Y. Ma, G.-F. Xu, X. Yang, L.-C. Li, J.-K. Tang, S.-P. Yan, P. Cheng and D.-Z. Liao, *Chem. Commun.*, 2009, **46**, 8264-8266.
8. T. T. da Cunha, J. Jung, M. E. Boulon, G. Campo, F. Pointillart, C. L. M. Pereira, B. L. Guennic, O. Cador, K. Bernot, F. Pineider, S. Golhen and L. Ouahab, J. *Am. Chem. Soc.*, 2013, **135**, 16332-16335.
9. M. Ji, M.-Y. Liu and S.-L. Gao, *Instrum. Sci. Technol.*, 2001, 29, 53-57.

10. (a) S.-L. Wang, L. Li, Z.-W. Ouyang, Z.-C. Xia, N.-M. Xia, T. Peng and K.-B. Zhang, *Acta Phys. Sin.*, 2012, **61**, 107601; (b) H. Nojiri and Z.-W. Ouyang, *Terahertz Sci. Technol.*, 2012, **5**, 1.
11. G. M. Sheldrick, SADABS, Program for Empirical Absorption Correction, University of Göttingen, Göttingen, Germany, 1996.
12. G. M. Sheldrick, SHELXS-2014 and SHELXL-2014, Program for Crystal Structure Determination, University of Göttingen, Göttingen, Germany, 2014.
13. (a) F. Neese, *Wiley Interdiscip. Rev.: Comput. Mol. Sci.*, 2012, **2**, 73-78; (b) F. Neese, *Wiley Interdiscip. Rev.: Comput. Mol.Sci.*, 2018, **8**, e1327; (c) F. Neese, ORCA-an Ab Initio, Density Functional and Semiempirical Program Package, 4.2.1, University of Bonn, Bonn, Germany, 2019.
14. (a) A. D. Becke, *Phys. Rev. A*, 1988, **38**, 3098-3100; (b) C. Lee, W. Yang and R. G. Parr, *Phys. Rev. B*, 1988, **37**, 785-789; (c) P. J. Stephens, F. J. Devlin, C. F. Chabalowski and M. J. Frisch, *J. Phys. Chem.*, 1994, **98**, 11623-11627.
15. F. Weigend and R. Ahlrichs, *Phys. Chem. Chem. Phys.*, 2005, **7**, 3297-3305.
16. P. A. Malmqvist and B. O. Roos, Chem. Phys. Lett., 1989,155, 189-194.
17. (a) C. Angeli, R. Cimiraglia, S. Evangelisti, T. Leininger and J. P. Malrieu, *J. Chem. Phys.*, 2001, **114**, 10252-10264; (b) C. Angeli, R. Cimiraglia and J. P. Malrieu, *Chem. Phys. Lett.*, 2001, **350**, 297-305; (c) C. Angeli, R. Cimiraglia and J. P. Malrieu, *J. Chem. Phys.*, 2002, **117**, 9138-9153; (d) C. Angeli, S. Borini, M. Cestari and R. Cimiraglia, *J. Chem. Phys.*, 2004, **121**, 4043-4049; (e) R. Herchel, I. Nemec, M. Machata and Z. Trávníček, *Dalton Trans.*, 2016, **45**, 18622-18634.
18. D. Ganyushin and F. Neese, *J. Chem. Phys.*, 2006, **125**, 024103.
19. F. Neese, *J. Chem. Phys.*, 2005, **122**, 034107.
20. (a) R. Maurice, R. Bastardis, C. Graaf, N. Suaud, T. Mallah and N. Guihéry, *J. Chem. Theory Comput.*, 2009, **5**, 2977-2984; (b) I. Nemec, R. Herchel, M. Machata and Z. TrávnÍček, *New J. Chem.*, 2017, **41**, 11258-11267.
21. F. Weigend, *Phys. Chem. Chem. Phys.*, 2006, **8**, 1057-1065.
22. (a) F. Neese, F. Wennmohs, A. Hansen and U. Becker, *Chem. Phys.*, 2009, **356**, 98-109; (b) R. Izsak and F. Neese, *J. Chem. Phys.*, 2011, **135**, 144105.
23. (a) J. Wu, S.-P. Chen and S.-L. Gao, *Mater. Chem. Phys.*, 2010, **122**, 301-304; (b) Y. Mi, Z.-Y. Huang, J.-Y. Jiang and Y.-F. Li, *Mater. Lett.*, 2011, **65**,1768-1771;(c) L.-D. Wang, Z. Ma, S.-G. Liu and Z.-Y. Huang, *J. Therm. Anal. Calorim.*, 2014,

115, 201-208; (d) J. Chen, Y. J. Ma, G.-C. Fan, Y.-F. Li, J.-Y. Jiang and Z.-Y. Huang. *Mater. Lett.*, 2011, **65**, 1768-1771.

24. (a) M.-H. Zeng, S.-H. Q. Chen, G. Xie, Q. Shuai, S.-L. Gao and L.-Y. Tang, *Inorg. Chem*., 2009, **48**, 7070-7079; (b) S. Fischer, G. Krahn and B. Reimer, *Thermochim. Acta*, 2006, **445**, 160-167.
25. J. F. Berry, F. A. Cotton, C.-Y. Liu, T. Lu, C. A. Murillo, B. S. Tsukerblat, D. Villagran and X. Wang, *J. Am. Chem. Soc.*, 2005, **127**, 4895-4902.
26. M. Llunell, D. Casanova, J. Cirera, P. Alemany and S. Alvarez, *SHAPE, v2.1*, 2013.
27. R. Boča, *Coord. Chem. Rev.*, 2004, **248**, 757-815.
28. (a) A. V. Palii, B. S. Tsukerblat, E. Coronado, J. M. Clemente-Juan, J. J. Borras-Almenar, *Inorg. Chem.*, 2003, **42**, 2455-2458; (b) A. V. Palii, B. S. Tsukerblat, E. Coronado, J. M. Clemente-Juan, J. J. Borras-Almenar, *J. Chem. Phys.*, 2003, **118**, 5566-5581.
29. R. L. Carlin, *Magnetochemistry*, Springer-Verlag, Berlin, 1986.
30. N. F. Chilton, R. P. Anderson, L. D. Turner, A. Soncini and K. S. Murray, *J. Comput. Chem.*, 2013, **34**, 1164-1175.
31. Y.-J. Zhang, L. Yin, J. Li, Z.-B. Hu, Z.-W. Ouyang, Y. Song and Z. Wang, *RSC Adv.*, 2020, **10**, 12833-12840.
32. D. V. Korchagin, A. V. Palii, E. A. Yureva, A. V. Akimov, E. Y. Misochko, G. V. Shilov, A. D. Talantsev, R. B. Morgunov, A. A. Shakin, S. M. Aldoshin and B. S. Tsukerblat, *Dalton Trans.*, 2017, **46**, 7540-7548.
33. R. Herchel, L. Váhovská, I. Potočňák and Z. Trávníček, *Inorg. Chem.*, 2014, **53**, 5896-5898.
34. R. Orbach, *Proc. R. Soc. London, Ser. A*, 1961, **264**, 458-484.
35. (a) K. S. Cole and R. H. Cole, *J. Chem. Phys.*, 1941, **9**, 341-351. (b) K. Suzuki, R. Sato and N. Mizuno, *Chem. Sci.*, 2013, **4**, 596-600.
36. (a) R. Herchel, I. Nemec, M. Machata and Z. Travnicek, *Inorg. Chem.*, 2015, **54**, 8625-8638; (b) J.-D. Leng, S.-K. Xing, R. Herchel, J.-L. Liu and M.-L. Tong, *Inorg. Chem.*, 2014, **53**, 5458-5466; (c) M. Machata, I. Nemec, R. Herchel and Z. Travnicek, *RSC Adv.*, 2017, **7**, 25821-25827.
37. A. Ghisolfi, K. Y. Monakhov, R. Pattacini, P. Braunstein, X. López, C. Graaf, M. Speldrich, J. Leusen, H. Schilder and P. Kögerler, *Dalton Trans.*, 2014, **43**, 7847-7859.